Insights into the mechanism of the gas-phase purification of HiPco SWNTs through a comprehensive multi-technique study†

Gaëlle Charron,*[a] Sandra Mazerat,[a] Mehmet Erdogan,[b] Alexandre Gloter,[b] Arianna Filoramo,[c] Julien Cambedouzou,[b] Pascale Launois,[b] Eric Rivière,[a] Wolfgang Wernsdorfer,[d] Jean-Philippe Bourgoin[c] and Talal Mallah*[a]

Received (in Montpellier, France) 9th January 2009, Accepted 26th March 2009
First published as an Advance Article on the web 27th April 2009
DOI: 10.1039/b900373h

While the purification of carbon nanotubes may be considered as an already sorted matter, their use in some highly demanding fields such as electrochemistry, biological studies or magnetism may be precluded by the remaining catalyst and carbonaceous impurities. For these purposes, the widely-used purification methods need to be improved. In this paper, a comprehensive study of the well-known gas-phase purification procedure of single wall nanotubes (SWNTs) is performed, which aims at depicting the nature and the amount of the remaining impurities, of both the catalyst and carbon types, and at getting insights into its mechanism. This has been achieved by cross-referencing data emerging from transmission electron microscopy (TEM), electron energy loss spectroscopy (EELS), electron diffraction, magnetization measurements, X-ray diffraction (XRD) and Raman spectroscopy. We demonstrate that this method can lead to the elimination of the largest part of the impurities while maintaining fairly good yields. According to the mechanistic picture we have drawn, we suggest some possible improvement to the procedure that should lead to fully purified SWNTs with limited subsequent losses.

Introduction

Carbon nanotubes (CNTs) have been extensively studied since their discovery in 1991 because of their extraordinary mechanical and electronic properties.[1] Single wall nanotubes (SWNTs) and numerous composite materials based on it have been achieved, with applications ranging from chemosensors[2–5] to drug delivery,[6–8] nanoelectronic devices[8–12] and high Young modulus fibers.[13–15] These applications have been made possible, and the composite materials they are based on have been successfully designed, thanks to the various types of purification procedures that allow for the elimination of most of the catalyst and carbonaceous impurities that are present in the raw material (up to 60 wt%).[16–27] However, in some applications the remaining traces of impurities can prevent the quantitative studies of carbon nanotube composites and their subsequent applications. For example, it has been demonstrated that remaining catalyst particles may have an electrochemical activity and disturb the assessment of redox processes on CNT-modified electrodes.[28–31] The catalysts used for the synthesis of CNTs are ferromagnetic and can thus prevent, even at very low concentration, the investigation of the intrinsic magnetic properties of magnetic materials based on CNTs.[32,33] Due to their potential commercial applications, CNTs have been the subject of many studies devoted to their biological impact.[34–36] These investigations have led to conflicting results, most probably because of the presence of ill-defined chemical species within the CNTs. The composition of the CNTs samples strongly depends on the methods of production and purification, and on the resulting CNTs size distribution, aggregation state, surface state and defects and catalyst particle concentration. Such highly sensitive and demanding applications require a detailed picture of the nature of the chemical species present in the purified CNTs material and need the purification methods to be improved.

To date, the studies dedicated to the purification of SWNTs have mainly focused on either the carbonaceous impurity or the metal content, but rarely on both simultaneously. In general, interests have been focused on the final purity rate, most of the time estimated either by thermogravimetric analysis, TEM or Raman spectroscopy. As recently stressed by Kolodiazhnyi and Pumera, these analytical techniques have different sensitivities towards different types of impurity.[30] Thus a more precise estimation of the level of purity is obtained when cross referencing the data emerging from several techniques applied to a unique sample. Kholodiazhni and Pumera reported such a multi-technique study of the gas-phase purification procedure of MWNTs, while focusing on the metallic impurities. A few years ago, Itkis *et al.* reported a multi-technique study dedicated to the evaluation of carbonaceous impurities in as-produced SWNTs.[37] To the

---

[a] *Institut de Chimie Moléculaire et des Matériaux d'Orsay, CNRS, Université Paris-Sud 11, 91405, Orsay Cedex, France. E-mail: gaellecharron@gmail.com, mallah@icmo.u-psud.fr; Fax: +33 1 69154754; Tel: +33 1 69154749*
[b] *Laboratoire de Physique des Solides, UMR CNRS 8502, Université Paris-Sud 11, 91405, Orsay Cedex, France*
[c] *Laboratoire d'Electronique Moléculaire, Service de Physique de l'Etat Condensé, CNRS URA 2464, CEA Saclay, 91191, Gif sur Yvette Cedex, France*
[d] *Institut Néel, Département Nanosciences, BP166, 25 avenue des Martyrs, 38042, Grenoble Cedex 9, France*

† Electronic supplementary information (ESI) available: Additional characterization data. See DOI: 10.1039/b900373h

best of our knowledge, a similar study devoted to both catalyst and carbonaceous impurities has not been reported for SWNTs, to date. Moreover, to improve the purification procedures, it is now necessary to have clear microscopic insights into their mechanisms and into their impact on the catalyst and carbonaceous impurities as well as on how they affect the nanotubes. Starting from such a mechanistic picture, optimization of the purification conditions could be achieved, leading to both enhanced purity and enhanced quality of the nanotubes.

In this paper, we report the systematic study of a multi-step gas-phase purification procedure derived from a previously reported protocol,[16] under the scope of local probes such as transmission electron microscopy (TEM), electron energy loss spectroscopy (EELS) and electron diffraction (ED), and of more global probes at the scale of a macroscopic sample such as magnetization measurements, X-ray diffraction (XRD) and Raman spectroscopy. These techniques provide information on both the amount of catalytic impurities and the carbonaceous impurities surrounding the SWNTs, for several steps of the purification process. The collected data allow us to suggest a plausible mechanism describing the purification process that leads to possible improvements of the procedure.

Experimental

The SWNTs were synthesized by the so-called HiPco process and purchased as the first purified grade from Carbon Inc. (Houston, Texas). The declared average diameter is 1.1 nm and the indicated carbon content in the pristine material is 87%. The multi-step gas-phase purification has been achieved by performing the following procedure. First, the oven was heated to 150 °C (4 °C $\min^{-1}$) and stabilized for 1 h at this temperature. The nanotubes were inserted into a Pyrex vial and heated in the furnace for 1 h under a flow of wet air. After cooling, the nanotubes were stirred in hydrochloric acid (37 wt%) for 100 min in an ultrasonic bath, while taking care to maintain the temperature of the media under 12 °C. The suspension was then filtered on a polytetrafluoroethylene (PTFE) nanoporous membrane (0.2 μm). The yellow filtrate was introduced in a volumetric flask and analysed by visible absorption spectroscopy. Finally, the nanotubes are dried by suction and put in an oven overnight (step **1**). The overall "heating–washing–drying" cycle was repeated with heating for 1 h at 200 °C (step **2**), 1 h at 250 °C (step **3**), 1 h at 250 °C (step **4**), 1 h at 300 °C (step **5**), 1 h at 300 °C (step **6**), 1 h at 350 °C (step **7**), 1 h at 350 °C (step **8**), 1 h at 400 °C (step **9**), 1 h at 450 °C (step **10**), 30 min at 470 °C (step **11**), 12 min at 490 °C (step **12**), 12 min at 500 °C (step **13**), 12 min at 500 °C (step **14**), 12 min at 510 °C (step **15**). Each sample is hereafter quoted by the number of the step that produced it.

UV-vis absorption analysis were performed on a Cary 300 spectrometer. Transmission electronic microscopy (TEM) images were recorded on JEOL 2100 apparatus. High annular angle dark field scanning electron microscopy (HAADF-STEM) and electron energy loss spectroscopy (EELS) experiments were performed on a STEM VG microscope equipped with a modified Gatan spectrometer. For these techniques, samples were prepared by casting a few drops of a dispersion of 0.5 mg of nanotubes in 2 mL of dichlorobenzene on hollow carbon lacey grids.

Magnetization measurements were performed on a Quantum Design MPMS SQUID magnetometer at 5 K. Samples were prepared by wrapping a few tenths mg of carbon nanotubes in about 15 mg of cling film. The known diamagnetic contribution of the film was subtracted of the magnetization curve of each sample.

XRD measurements were recorded in transmission on a planar imaging plate under vacuum in order to minimize air scattering. The Kα radiation of a Mo rotating anode (λ = 0.711 Å) was used in order to prevent fluorescence from iron particles in the SWNT samples. An aluminium foil was used as sample holder to minimize the signal from the container in the 0.2–2.5 Å^{-1} range, where diffraction peaks from the bundled structure of SWNTs are expected. When we considered the 2.5–8 Å^{-1} range where diffraction peaks are expected from iron-based phases, we preferred using glass capillaries.

Raman spectra were collected on a T64000 Jobin-Yvon triple spectrometer, accessorized with an optical microscope, using a Ar laser as the excitation source. The diameter of the beam was equal to 2 μm. The sample was prepared by filtering freshly sonicated dispersions of nanotubes on polycarbonate nanoporous membranes. For each sample, four spectra were recorded at 488.0, 514.5, 568.2 and 647.1 nm excitation wavelengths, at two distinct points of the sample. The excitation power was set up in between 0.3 and 0.7 mW to restrict the heating of the samples. The temperature of the room was stabilized at 23 °C. The spectra were calibrated using a silicium wafer prior to each acquisition.

Results and discussion

Yields and iron extraction rate

The catalyst impurities present in the raw carbon nanotubes cannot be removed by simple acidic washing because of the presence of carbon shells around the catalyst particles. The principle of the gas-phase purification procedure is based on the oxidation by air of these protective carbon shells catalysed by the metallic particles, as reported by Chiang *et al.*[16] The catalysis of the oxidation of these carbon shells allows the exposure of the bare catalysts, which render their elimination by solubilization in acidic media possible.[16] The higher the temperature, the more efficient the removal of the catalyst particles. Unfortunately, bare catalysts particles also catalyse the parasitic oxidation of carbon nanotubes. This parasitic reaction becomes noticeably efficient at around and above 400 °C. To avoid combustion of the nanotubes during their purification, a first annealing is generally performed at a moderate temperature (around 200 °C), followed by dissolution of the bare catalyst in a non-oxidizing acid such as HCl. The heating–washing procedure is usually repeated several times with increasing heating temperatures. The progressive removal of the catalyst during the procedure limits the loss of nanotubes due to their catalyzed parasitic oxidation. Table 1 summarizes the yields and cumulative yields after each step of the procedure we followed. The yields

Table 1 Yields and cumulative yields of the different purification steps

Step (T/°C, t/min)	Yield of step (%)	Cumulative yield (%)
1 (150, 60)	93	—
2 (200, 60)	97	89
3 (250, 60)	93	84
4 (250, 60)	94	78
5 (300, 60)	90	70
6 (300, 60)	97	68
7 (350, 60)	81	55
8 (350, 60)	93	51
9 (400, 60)	65	33
10 (450, 60)	48	16
11 (470, 30)	96	15
12 (490, 12)	33[a]	5[a]
13 (500, 12)	—	—
14 (500, 12)	—	—
15 (510, 12)	—	—

[a] Calculated for steps 12–15.

are about 90% or more for each step until step **9** at which point the oxidation of the nanotubes becomes very efficient. After step **15**, the yield drops to 5%. This might be due to a very effective oxidation of the nanotubes as well as losses on glassware due to handling of very small amounts of material. For the double steps at 300, 350 and 450–470 °C (**5**–**6**, **7**–**8** and **10**–**11**), the iron extraction rate (obtained from the UV-visible titration of $FeCl_4^-$)[38] of the second step is smaller than that of the first, while the yield in carbon is greater (Fig. 1), suggesting that fewer bare particles are produced during the second step than during the first. This indicates that there is a distribution of reactivity towards oxidation within the particles. Some of them are oxidized immediately during the low temperature steps, while others are eliminated only at higher temperatures. It is to note that the total amount of extracted iron after step **11** corresponds to 16 wt% of the starting material, which indicates that the purity level of 87% of the starting material has been slightly overstated, as previously outlined by recent purification reports.[37,39]

TEM, HAADF-STEM and EELS studies

The pristine nanotubes and the purified nanotubes resulting from steps **1**, **3**, **8**, **10** and **15** have been examined by TEM, HAADF-STEM and EELS.

Study of the catalyst impurities. TEM images at low magnification of the pristine sample reveal bundles of nanotubes abundantly decorated by dark spots, encompassing heavy elements that efficiently scatter the electron beam and are thus displayed by a high contrast (Fig. 2). These dark spots correspond to iron catalyst particles. Two main size populations are distinguished, with diameters ranging from 3–6 nm for a large majority and from 10–20 nm for a minority of particles. HAADF-STEM images display similar information, with white spots corresponding to metal particles densely covering lightly contrasted bundles of nanotubes (Fig. 3). The concentration of catalyst particles seems higher on the dark field images because this technique is more sensitive to the atomic weight of the imaged elements. The catalyst particles can be bare (Fig. 4), encapsulated within a simple carbon shell (Fig. 5) or within multiple layered carbon shells of various thicknesses (Fig. 6). Sample **3** (collected after step **3**) reveals a lower concentration of catalyst particles (Fig. 7). In the HAADF-STEM mode, EELS spectra of two particles (denoted A and B) have been recorded providing information on their chemical composition (Fig. 8). The presence of iron is assessed by a doublet of peaks centered at 715 eV superimposed on a continuum of transitions. These peaks

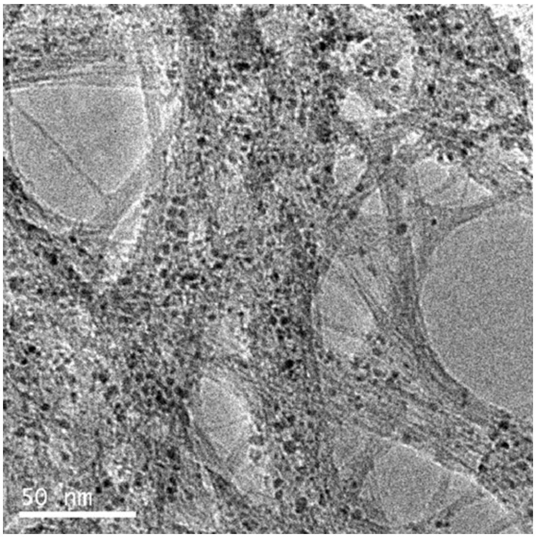

Fig. 2 TEM image of the pristine nanotubes at intermediate magnification (scale bar: 50 nm).

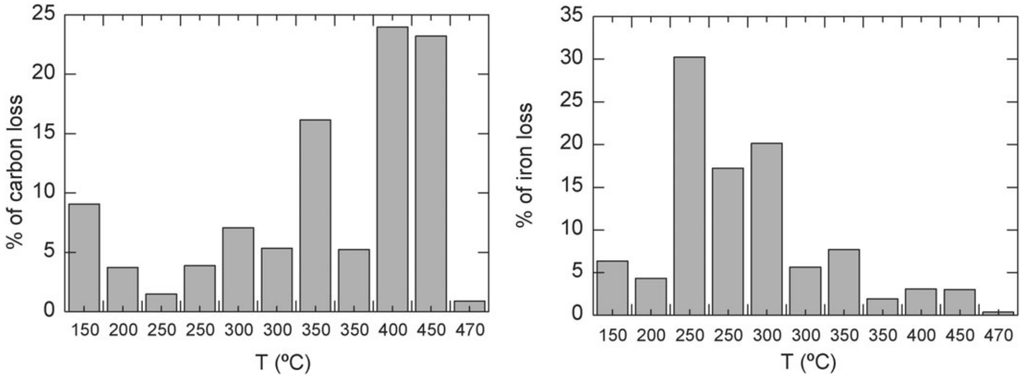

Fig. 1 Overall percentage of carbon and iron loss calculated for a given step.

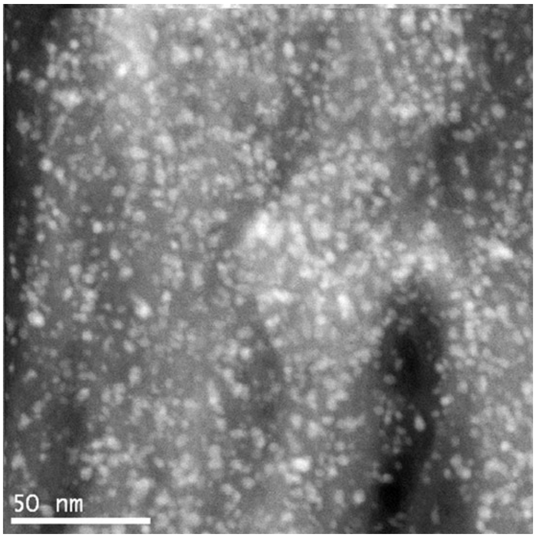

Fig. 3 HAADF-STEM at intermediate magnification of pristine nanotubes (scale bar: 50 nm).

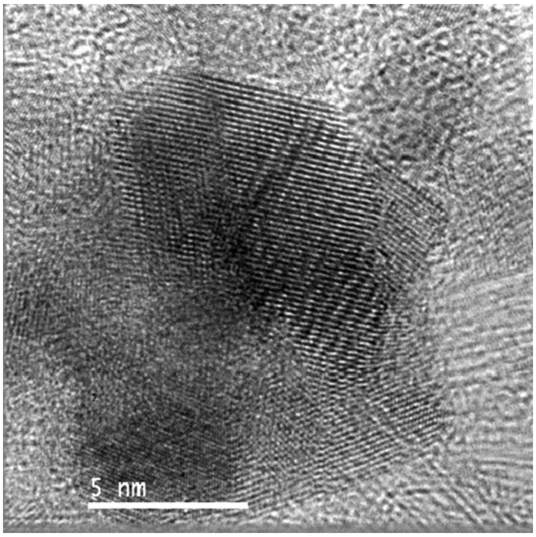

Fig. 4 HRTEM image of bare particles (pristine nanotubes, scale bar: 5 nm).

correspond to transitions from the Fe 2p core levels to the Fe 3d levels that are characterized by a narrow energy dispersion. The observed splitting is due to the spin–orbit coupling within the 2p levels leading to the $2p_{3/2}$ and $2p_{1/2}$ transitions. The continuum of transitions corresponds to excitations of 2p electrons to strongly delocalized 4s and 4d levels. At high energy resolution (<0.3 eV), it is generally possible to observe a sub-splitting of the two peaks due to the crystal field and thus to obtain information on the valency and the environment of the metal.[40] In the present case, the spectra have been recorded so as to simultaneously obtain edges ranging from 100 to 800 eV, with an energy resolution of about 1 eV, preventing the resolution of the crystal field splitting. However, the profile of the edges allows the differentiation between oxidized and non-oxidized metallic centres. For oxidized iron, the intensity of the Fe $2p_{3/2}$ transition ($H_{\max}$) is strongly enhanced when compared to that of the continuum that can be estimated from the height of the signal between the two peaks (H_{centre}, Fig. 8). With a comparable energy resolution, a set of different iron oxide samples (haematite, goethite, siderite, FeOOH) of various thicknesses has provided an average $H_{\max}/H_{\text{centre}}$ ratio of 6.5, with values within the range 4–8, while pure iron samples gave an average ratio of 2.85, with values ranging from 2.4 to 3. These ratios are not to be considered absolute since they depend on the energy resolution and on the thickness of the sample. However, they may be used qualitatively as an indication of the oxidation state of iron in the catalyst particles. The iron phases to be expected include pure iron and, taking into account the temperatures used during the purification steps, magnetite ($Fe^{II/III}$) and maghemite (Fe^{III}). In addition, as previously demonstrated by Gavillet *et al.*, the

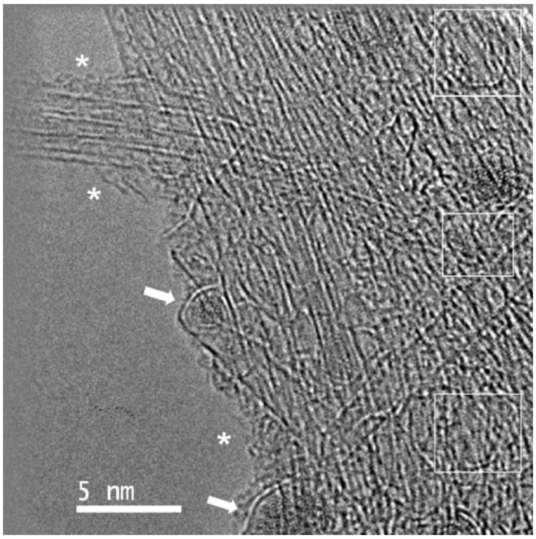

Fig. 5 HRTEM image of particles encapsulated in single carbon shells (pristine nanotubes, scale bar: 5 nm), white arrows, stars and insets emphasize particles encapsulated in a single shell, amorphous carbon and empty graphitic shells, respectively.

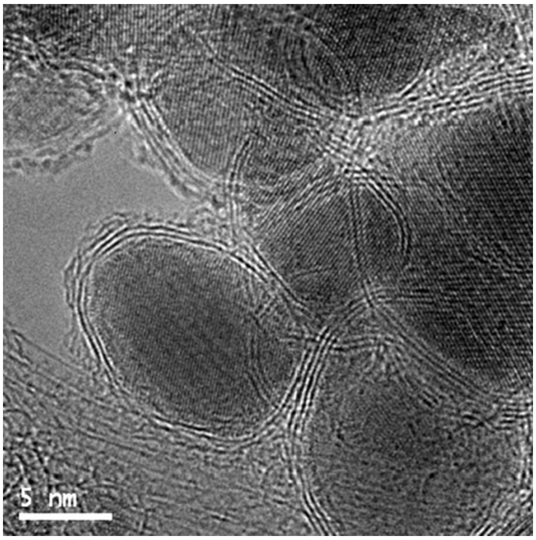

Fig. 6 HRTEM image of particles encapsulated in multiple carbon shells (pristine nanotubes, scale bar: 5 nm).

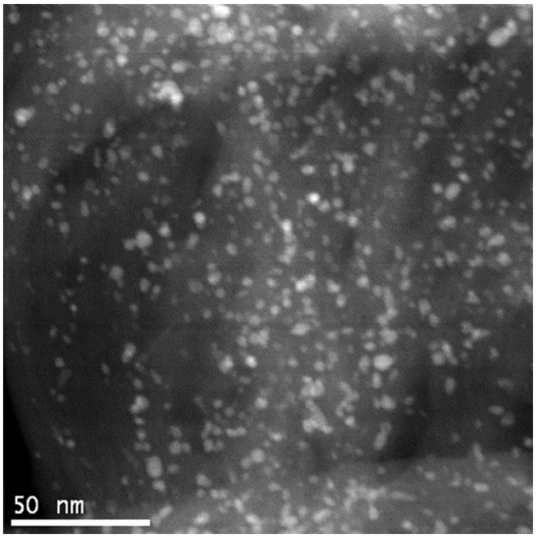

Fig. 7 HAADF-STEM image of nanotubes **3** at intermediate magnification (scale bar: 50 nm).

nucleation and growth processes of SWNTs start from iron carbide particles (Fe_3C).[41] In this phase, the formal oxidation state of iron is +0.33 and the extent of covalency is high. A H_{max}/H_{centre} ratio close to the value of pure iron can be expected and should be easily differentiated from that of an oxidized phase such as maghemite or magnetite. The spectra have been analysed using the following criterion: a H_{max}/H_{centre} ratio less than 3 corresponds to a metallic or carbide phase, and to an oxidized phase if larger. Thus, with a H_{max}/H_{centre} ratio of 2.77, the particle **A** is mainly metallic, whereas the H_{max}/H_{centre} ratio of 5.68 for the particle **B** indicates an oxidized phase. These results are further confirmed by the presence of a peak at 530 eV corresponding to the 1s edge of oxygen in the spectrum of **B**, which is absent in the spectrum of **A**. This peak presents a pre-edge characteristic of oxygen coordinated to transition metals.[42] The different oxidation states of both particles may be explained in terms of the particle size. As the particle **B** is smaller, the diffusion of oxygen may have been driven to completion during the exposure time in the oven, while for the larger particle **A**, the oxygen has not reached the core during the purification step. This analysis of the oxidation states has been repeated for several particles on different parts of the sample (Fig. S1, ESI†). Both metallic and oxidized particles are found in comparable proportions. Some particles have been oxidized during the purification step, whereas others have been resistant to the oxidative conditions, even though in most cases their sizes are similar. This confirms that there is a distribution of reactivity towards oxygen within the particles' population. Many particles with a toroidal shape, *i.e.* hollow particles, are found in the samples (Fig. 9). They consist of oxidized iron, as demonstrated by a H_{max}/H_{centre} ratio of 5.95. The O 1s edge presents a pre-edge characteristic of oxygen coordinated to transition metals. The presence of a graphite-like C 1s edge (Fig. 9) indicates that they are still surrounded by a carbon shell.[43] The formation of the toroidal particles is probably due to an incomplete removal (after washing) of the oxide core because of the presence of the carbon shell. The presence of such particles at step **3** suggests that during the purification step the metal core is fully oxidized prior to the carbon shell. This observation will be determinant for the purification mechanism proposed below.

Another interesting feature of sample **3** is the occurrence of a noticeable change of the size distribution of the particles. The relative amount of 10–20 nm particles has increased compared to the 3–6 nm particles (Fig. 10). The larger particles present few shells of carbon with a low curvature (Fig. S2, ESI†). Several bunches of about 100 nm width, consisting of particles with diameters from 10 to 20 nm, appear in the low magnification STEM images (Fig. 11). They have not been detected during the previous steps probably because of a weak contrast difference with the nanotubes heavily decorated by individual particles.

After step **8**, the concentration of catalyst particles has dramatically decreased (Fig. 12 and Fig. 1). The major impurity population now consists of bunches of particles with diameters from 10 to 20 nm (Fig. 13). The toroidal particles are no longer detected. EELS spectra of the remaining 3–6 nm particles indicate metallic or carbide phases. The particles

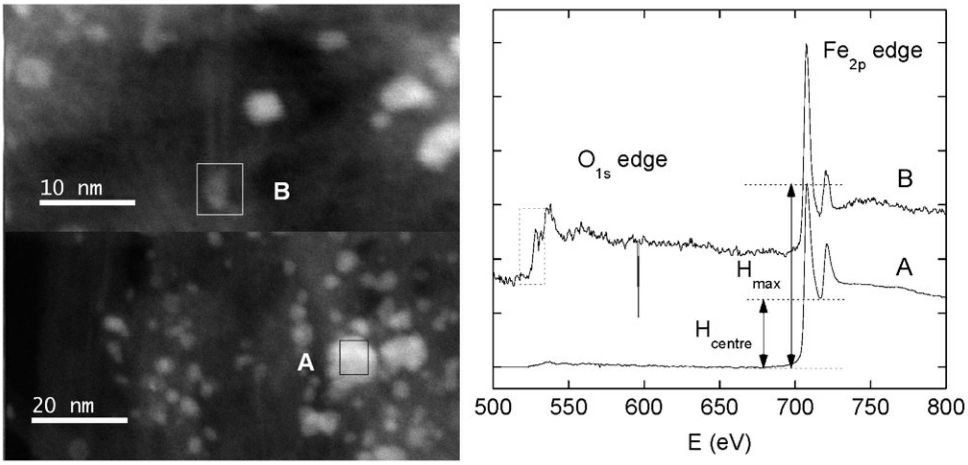

Fig. 8 HAADF-STEM images of two particles **A** and **B** at high magnification (scale bar: 10 nm) and corresponding EELS spectra in the O 1s an Fe 2p edges range.

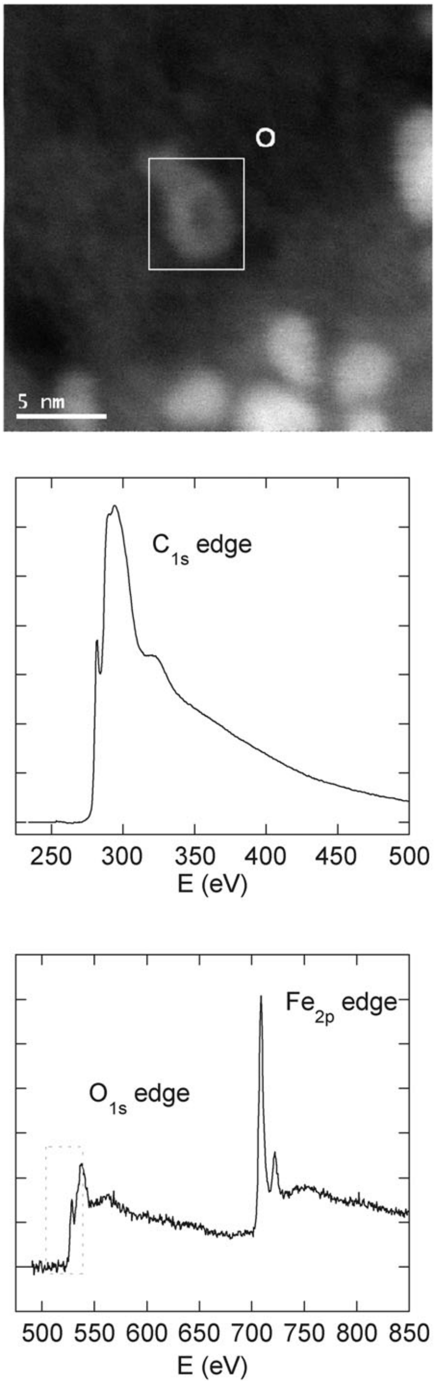

Fig. 9 HAADF-STEM image at high magnification of a toroidal catalyst particle in sample **3** (scale bar: 5 nm), and EELS spectra focusing on the C 1s, O 1s and Fe 2p edges of the toroidal particle.

belonging to the bunches also consist of non-oxidized iron phase (Fig. S3, ESI†). They are encapsulated in thick multiple layers of carbon, with an average number of seven graphitic shells, that is to say 2.4 nm of carbon protection (Fig. 14). Some particles are surrounded by only two or three carbon shells and display almost flat vertices (Fig. S4, ESI†). The particles gather in bunches because they are embedded into graphitic ribbons (Fig. S5, ESI†). In order to get an insight into the nature of the iron phase of these particles, a electron diffraction pattern has been recorded in the TEM microscope on a bunch consisting of about 100 particles (Fig. S6, ESI†). The first diffraction ring presents numerous diffraction spots, thus instantly discarding the highly symmetrical body-centred cubic (bcc) iron phase. The main peaks are finally attributed according to the *Pnma* structure of cementite (Fe_3C). The bunches of particles therefore consist of iron carbide.

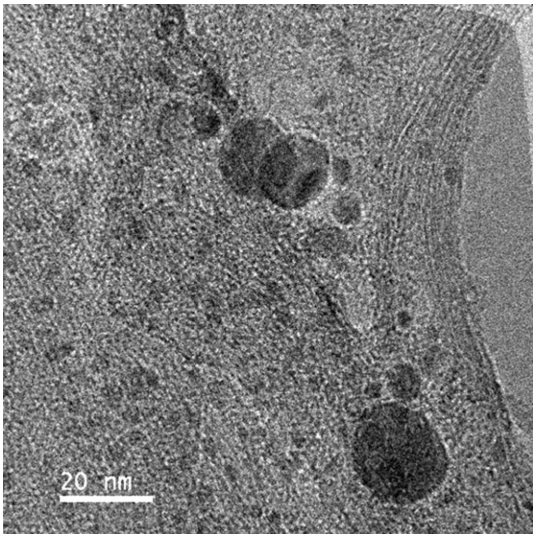

Fig. 10 TEM image at intermediate magnification of the nanotubes from sample **3** (scale bar: 20 nm).

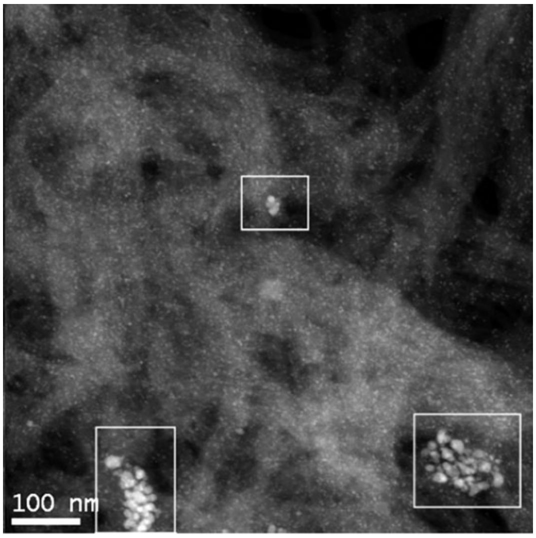

Fig. 11 HAADF-STEM image of nanotubes from sample **3** at low magnification, highlighting several bunches of catalyst particles (scale bar: 100 nm).

Sample **10** displays images that are similar to sample **8**. The particles with sizes ranging from 3 to 6 nm have almost completely disappeared (Fig. S7, ESI†). Most of the remaining isolated particles on nanotubes belong to the 10–20 diameter population and are mainly in a non-oxidized state (Fig. S8, ESI†). The sample still contains bunches of particles consisting of non-oxidized iron carbide (Fig. S9, ESI†). Sample **15** reveals an almost complete removal of the catalyst particles (Fig. 15).

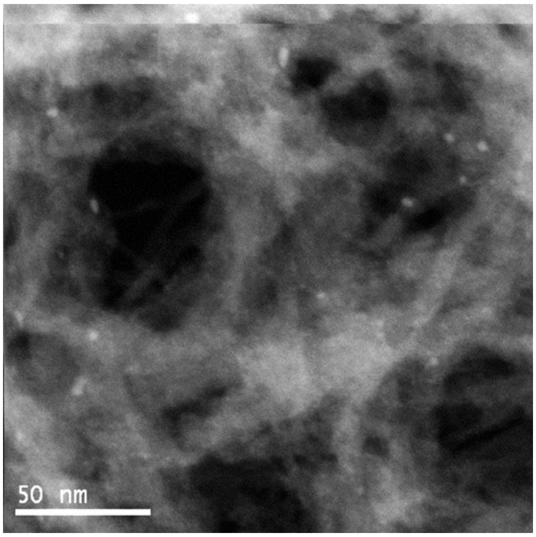

Fig. 12 HAADF-STEM image at intermediate magnification of sample **8** (scale bar: 50 nm).

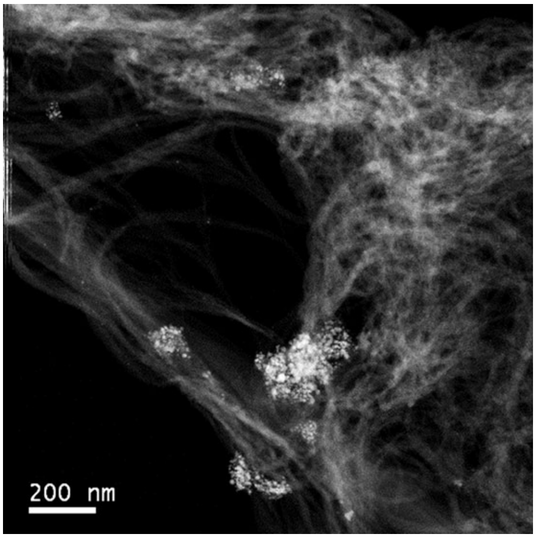

Fig. 13 HADF-STEM image at low magnification of sample **8** evidencing large bunches of catalyst nanoparticles (scale bar: 200 nm).

Most of the remaining isolated particles are oxidized, though some still display a metallic type EELS spectrum. The bunches of particles are still present, though they are far less predominant. According to the local EELS spectra, the particles belonging to bunches have been oxidized (Fig. 16).

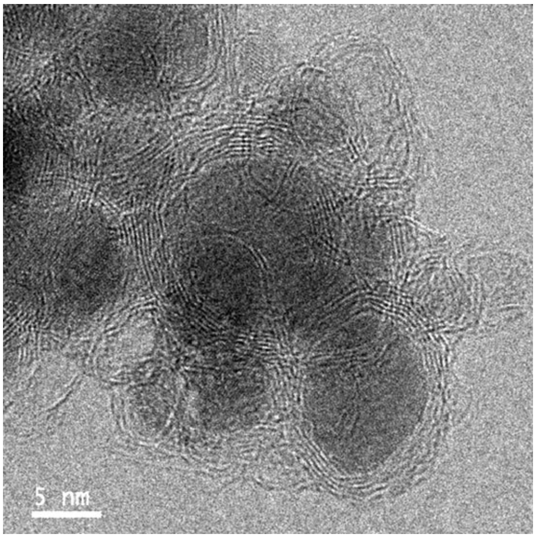

Fig. 14 HRTEM image of a bunch of catalyst particles in sample **8** (scale bar: 5 nm).

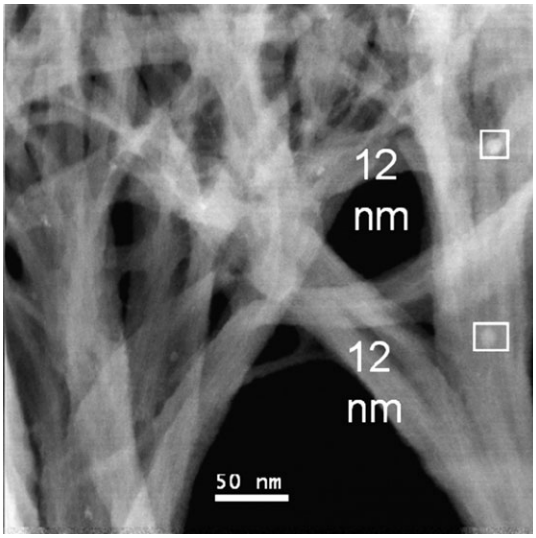

Fig. 15 HAADF-STEM image at intermediate magnification of sample **15** (scale bar: 50 nm).

Study of the surface of the nanotubes. HiPco nanotubes present, in general, less carbonaceous impurities than their counterparts synthesized by electric arc discharge. In the pristine nanotubes, these impurities are detected in bright field images on the surface of the bundles as amorphous carbon fragments and empty graphitic shells (Fig. 5). During the purification process, these impurities are progressively removed while the surface of the bundles becomes more and more regular and smooth (Fig. 17–19). In sample **15**, empty graphitic shells and amorphous carbon spots are no longer detected. Electron microscopy images, and especially HAADF-STEM images show that the overall extent of organization within the bundles increases step after step (Fig. 3 and Fig 5; Fig. 7, Fig. 10 and Fig. 17; Fig. 12 and Fig. 18; Fig. 16 and Fig. 19). This may be correlated to an enhanced van der Waals cohesion within the bundles due to the removal of amorphous carbon. EELS spectra of sample **15** recorded on the surface of nanotube bundles display carbon edges that are weakly structured, thus evidencing that a sub-nanometric layer of amorphous carbon remains on the sidewalls of the nanotubes after purification (Fig. S10, ESI†).[43] A similar covering of purified SWNTs by polyaromatic fragments has been recently demonstrated by Salzmann *et al.*[44] In addition, Si 1s edges are detected in the surface spectra of sample **15** (Fig. S10, ESI†). This silicium is most probably present as silica and may arise from the sublimation of the glass vial used for annealing or from traces of silicon grease in the oven.

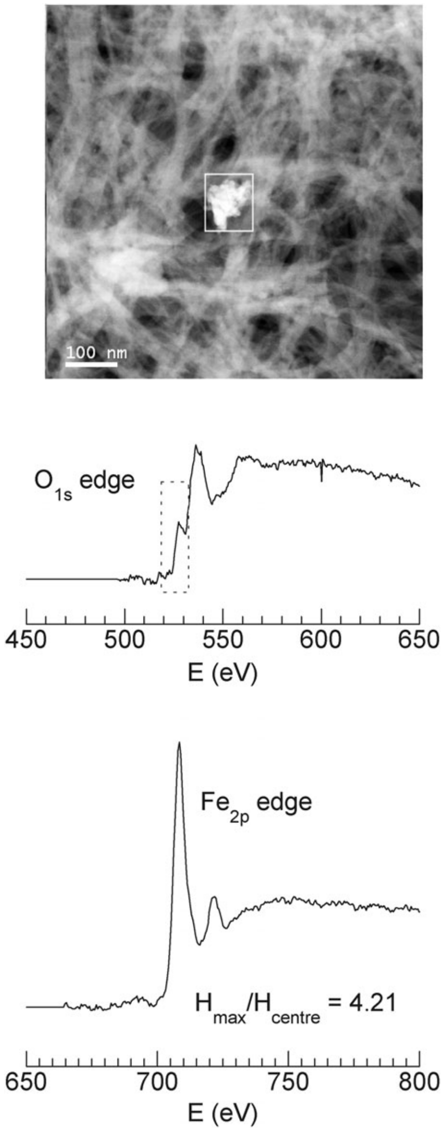

Fig. 16 HAADF-STEM image at low magnification of sample **15** (scale bar: 100 nm), and EELS spectra in the O 1s and Fe 2p edge area of the bunch of particles.

Magnetization measurements

The magnetization curves as a function of the applied magnetic field have been recorded at 5 K for the pristine, **3**, **8**, **10**, **13** and **15** nanotube samples. In each case, the magnetic signal is dominated by the signal of the catalyst impurities and a hysteresis loop is observed. As could have been expected from the decrease of the particle concentration observed by electronic microscopy, the saturation magnetization decreases during the purification process. Noticeably, the magnetization follows an exponential decay (Fig. 20). On the contrary, the coercitive field describes a complex evolution (Fig. 21). It increases from the pristine nanotubes to sample **8**, drops until sample **10**, then increases again until sample **13** and finally decreases until sample **15**. The phases that may be present in the samples include metallic iron, iron carbide and, taking into account the temperatures used in the purification steps, magnetite (Fe_3O_4) and maghaemite (γ-Fe_2O_3). All these compounds have Curie temperatures well above room temperature. Pure iron and cementite are ferromagnetic and have coercitive fields at room temperature of about 1 Oe and 8 Oe, respectively. Magnetite and maghemite are ferrimagnetic with coercitive fields at room temperature of 75–150 and 305–335 Oe. Nanoparticles of maghemite and magnetite have coercitive fields of about 300 Oe at 5 K.[45,46] To the best of our knowledge, no reliable data for pure iron nanoparticles are available because the metallic core is always surrounded by an oxide shell. In fact, when a source of carbon is present for the synthesis of iron nanoparticles, iron carbide particles are usually obtained, and they possess graphitic shells, as observed for the catalyst impurities present in the nanotube samples. Particles with sizes ranging from 10 to 20 nm have coercitive fields of 10 to 45 Oe.[47–49] However, after annealing in air, the coercitive field is found to increase up to 468 Oe.[47] Larger

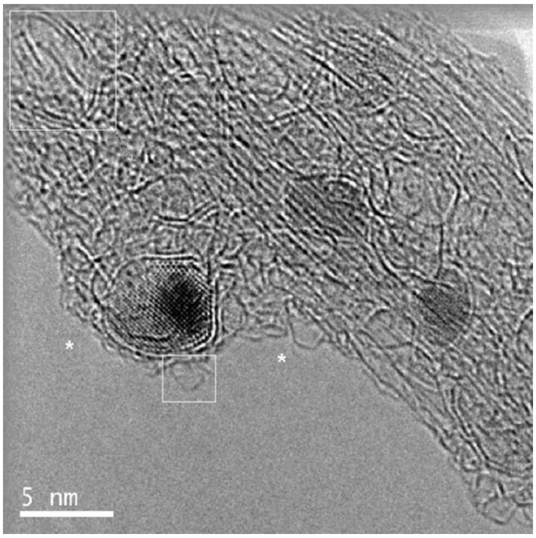

Fig. 17 HRTEM image of sample **3**. White rectangles indicate empty graphitic shells, whereas stars emphasize areas rich in amorphous carbon (scale bar: 5 nm).

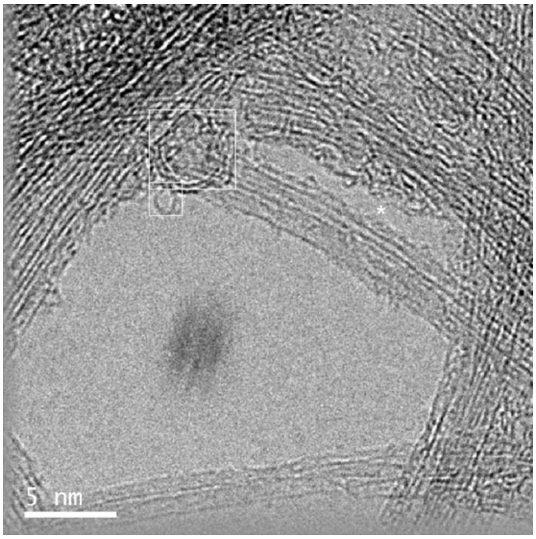

Fig. 18 High-magnification HRTEM image of sample **8**. White rectangles indicate empty graphitic shells, whereas stars emphasize areas rich in amorphous carbon (scale bar: 5 nm).

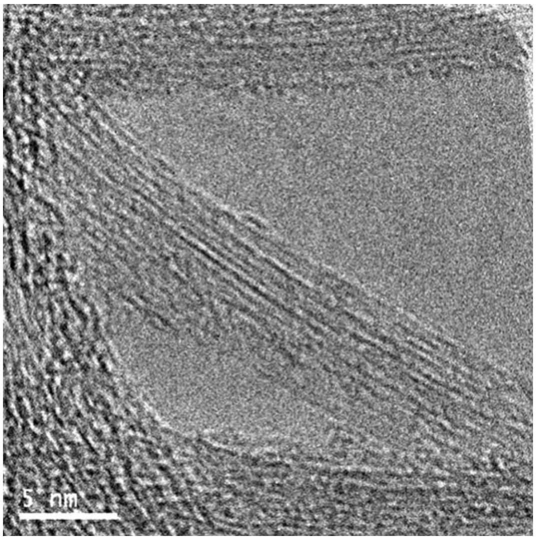

Fig. 19 High-magnification HRTEM image of sample **15** (scale bar: 5 nm).

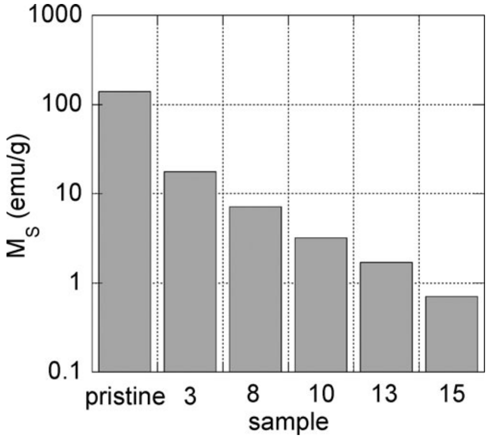

Fig. 20 Saturation magnetisation (M_S) at $T = 5$ K and $\mu_0H = 5.5$ T of the pristine and **3**, **8**, **10**, **13** and **15** purified samples.

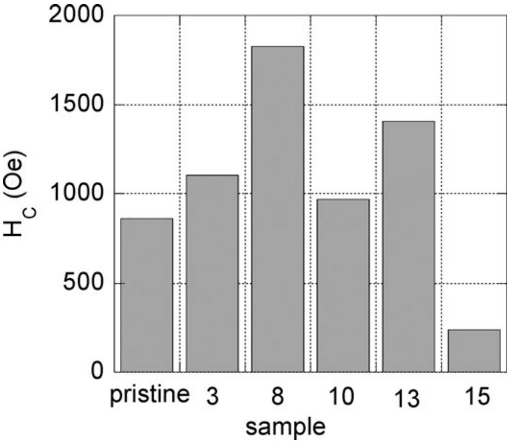

Fig. 21 Coercitive field (H_C) at $T = 5$ K of the pristine and **3**, **8**, **10**, **13** and **15** purified samples.

particles with sizes from 30 to 50 nm have a coercitive field of 867 Oe. However, depending on the synthetic protocol, thicker graphitic layers can be obtained, which lead to a weaker coercitive field (413 Oe).[50] Lee *et al.* have passivated their particles, thus building an iron oxide shell in between the iron carbide core and the graphitic layer. The measured coercitive fields vary from 788 to 500 Oe for diameters of 30 and 50 nm, respectively.[51] Such experimental observations can be understood from the results obtained by Shavel *et al.*[52] This group has recently investigated the magnetic properties of core–shell type iron@iron oxide nanoparticles with diameters of 10 nm. A coercitive field of 2000 Oe at 5 K has been recorded. The large coercitivity has been explained in terms of a spin disorder at the interface between the ferrimagnetic shell and the ferromagnetic core. According to this hypothesis, the volume ratio between the interfacial layer and the core should control the magnetic properties of the nanoparticle. Consequently, the presence of an iron oxide shell should lead to higher coercitivity. In addition, particles with smaller diameter and thus a higher surface/volume ratio should have larger coercitive field. The results of Shavel and co-workers allow us to consistently depict the evolution of the coercitive field in the pristine and purified nanotube samples. In the pristine nanotubes, the coercitive field of 860 Oe corresponds to a distribution of partially oxidized particles, including bare and weakly encapsulated particles, and non-oxidized particles, including particles encapsulated in thick or defect-free carbon shells. With a coercitive field of 1900 Oe, the catalyst impurities of sample **8** look very similar to the core–shell particles of Shavel and co-workers. Thus, from the pristine nanotubes to sample **8**, the coercitive field increases because an oxide layer is growing on the encapsulated particles, as evidenced above by EELS analysis. The decrease of the coercitive field after step **10** can be attributed to the almost complete removal of the smaller particles observed by TEM and HAADF-STEM. The increased coercitive field in sample **13** is correlated to the creation of a new population of particles bearing oxide shells, in agreement with the previous observed oxidation of the heavily encapsulated particles belonging to bunches between step **10** and **15**. The smaller coercitive field in sample **15** may arise from the fact that a large part of the partially oxidized particles belonging to bunches has been either removed or thoroughly oxidized during the last step. The evolution of the coercitive field is fully consistent with the microscopy observations of the samples taken from the different steps and with the presence of two particle populations showing different reactivities during the purification process.

X-Ray diffraction studies

Study of the catalyst impurities. XRD measurements have been performed on the pristine nanotubes and the purified samples **4**, **8**, **10** and **11**. This technique is efficient for the identification of iron-based phases in multi-walled nanotubes samples grown by CVD.[53] A quantification of the decrease in the concentrations of these iron rich phases is precluded because the density of the material varies upon the successive purification steps. Considering the rather low concentration in each iron-based phase involving peaks of weak intensity on one hand, and the nanometric size of these particles involving an enlargement of the peak width on the other hand, the diffraction peaks from iron particles are very difficult to observe. It is however possible to distinguish some of these peaks in the diffraction pattern of pristine SWNT as shown in Fig. S11 of ESI,† and further identify them. Diffraction peaks corresponding to Fe_3C (2.65, 3.35 and 4.47 Å^{-1}), Fe_3O_4 or γ-Fe_2O_3 (2.4 Å^{-1}) and γ-Fe (3.5 Å^{-1}) can be observed, the most intense peaks corresponding to cementite (Fig. S11, ESI†). When purified samples are considered, these peaks become less and less visible, and phase identification becomes less certain. The peaks corresponding to cementite are nevertheless clearly detected until step **11**, consistent with the electron microscopy results (Fig. 16).

Study of organization within the bundles of nanotubes. The samples conditioned in aluminium envelopes allow the recording of the diffraction pattern of the two-dimensional (2 D) hexagonal network of the nanotubes within the bundles. The powder diagram of the pristine nanotubes is poorly structured, therefore suggesting a weak organization within the bundles (Fig. 22). During the purification procedure, a structure emerges more and more clearly, indicating a progressive enhancement of the crystallinity within the bundles. Eventually, four diffraction peaks are detected in the powder diagram of sample **11**. The peak at 0.49 Å $^{-1}$ can be attributed to the first diffraction peak of first neighbours, *i.e.* the 10 peak of the 2 D hexagonal nanotube network. This allows a modelisation of the diffraction profile to be done using the formalism described elsewhere.[54] Our calculation was consistent with the experimental pattern considering an average value of the nanotube diameters of 1.16 nm in agreement with the commercial indications—a diameter distribution of FWHM 0.15 nm and small bundles having a radius of 3 nm. This enhancement of the crystallinity with the purification degree is consistent with the improvement of the organization within the bundles observed by HAADF-STEM and the lowering of the amount of amorphous carbon observed by HRTEM.

Raman spectroscopy

In a number of studies related to carbon nanotubes, Raman spectroscopy has been used to probe the nature and concentration of the carbon impurities thanks to the defect mode (D-mode). Previously, estimations of the chirality distribution within nanotubes have been extracted from the multifrequency analysis of the radial breathing mode (RBM). We performed a multi-frequency analysis of the pristine nanotubes and of samples **1**, **4**, **7**, **9** and **11** that allows for the estimation of the carbon impurity amount and the chirality distribution along the purification process.

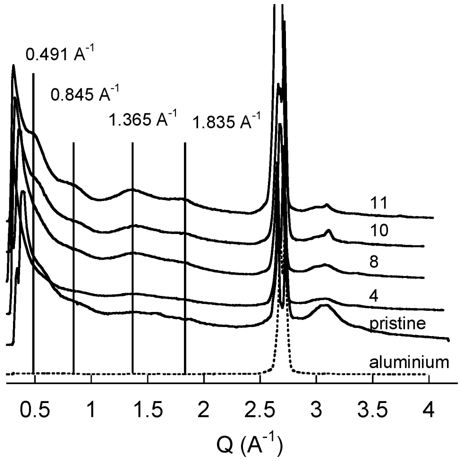

Fig. 22 XRD patterns of the pristine and **4**, **8**, **10** and **11** samples contained in aluminium envelopes.

Study of the carbonaceous impurities. The Raman D-band of SWNTs arises from a double resonance process assisted by defects and is generally observed for all forms of defective carbonaceous materials.[55,56] It is well known that the behaviour of this mode (frequency, position and intensity) is a function of the laser excitation energy.[57] The observation of the different features of the D-mode at 647, 514 and 488 nm along the purification process gives information on both the nature and the amount of carbonaceous impurities in the SWNTs samples (Fig. S12, ESI†). The shape of the D-mode is sensitive to the nature of the carbon impurity within the sample, with widths of 86, 57 and 6 cm^{-1} for graphite, amorphous carbon and isolated nanotubes, respectively.[58] The spectra of the pristine nanotubes display D-mode linewidths between 45 and 65 cm^{-1} that may correspond to the convolution of graphite and amorphous carbon impurities, consistently with our HRTEM observations. For a fixed wavelength, the D-mode linewidth shows no significant variations upon several oxidation steps in air, in contradiction with the narrowing of the D-mode previously observed in air oxidation processes.[58,59] Thus, the purified **11** sample still contains both graphitic and carbonaceous impurities. Moreover, for a given excitation wavelength, the position of the maximum of the D-mode is invariant upon the different purification steps. This indicates that the nature of the resonant impurities is not modified upon purification.

According to Dillon *et al.*, the intensity of the G mode compared to the D mode decreases when defects are introduced on the sidewalls of nanotubes.[58] During the purification process, the G/D ratio at 647 nm remains constant, while it increases by 33% and 150% at 514 and 488 nm, respectively. Several suggestions may be made at this point. First, the oxidative procedure used here does not introduce additional defects on the carbon nanotubes, in contradiction with the general increase of defect density observed with wet oxidative methods.[25] Furthermore, some carbonaceous impurities have been destroyed during the purification process, consistent with the removal of amorphous carbon observed by HRTEM. Eventually, the impurities that are resonant at 647 nm are less affected by the purification than those at 514 nm and to a greater extent that at 488 nm. This suggests that there is a distribution of reactivity within the carbonaceous impurities and that the purification method used here is not suitable for the removal of all types of impurities.

Study of the chirality distribution. The radial breathing mode of a carbon nanotube reflects a coherent dilatation of the carbon skeleton around its axis.[60,61] For a given excitation wavelength, the RBM frequencies of resonant nanotubes depend on both the diameter and the chiral angle of the nanotubes. These dependences have been presented in the so-called Kataura plots calculated using the extended tight binding model.[62,63] Thus, by recording the Raman spectra of a sample for a large range of excitation wavelengths and attributing the RBM peaks with the Kataura plots, a global picture of the chiralities present in the sample can be drawn.[64,65] The effect of the purification process on the chirality distribution of the nanotubes has been investigated following this method, by recording spectra at 647, 568, 514 and 488 nm. This combination of wavelengths allows us to probe most of the nanotubes with diameters ranging from 0.8 to 1.5 nm, a domain that should be well suited to our starting material according to the supplier and to our XRD studies (see above).

Recently, Miyata *et al.* performed a similar photoluminescence (PL) and Raman analysis of the effect of a gas-phase purification procedure on the chirality distribution of HiPco SWNTs.[65] They observed a decrease of the PL and Raman intensities of nanotubes with small diameters and high chiral angles, which they further assessed to a selective oxidation of these nanotubes upon purification. We indeed observed such a lowering of the Raman intensity of this type of nanotubes, the main feature being the large decrease of the intensity of the semi-metallic (8,5) nanotube (diameter: 0.89 nm, chiral angle: 22.41°) (Fig. 23). However, the relative concentrations of the different chiralities cannot unambiguously be estimated from the relative intensities of the RBM peaks. Actually, the resonant Raman cross section of a nanotube for a given wavelength depends on the level of matching between the incident or scattered energy and the energy of the transition between the closest Van Hove singularity,[61] and more importantly on the correspondent electron–phonon matrix element.[66,67] This last factor depends on the nanotube diameter, chiral angle and chiral index.[68] Thus, the recorded intensity of a RBM peak reflects both the concentration of the nanotube and its cross section. A calculation of the cross section of each SWNT is possible within the tight binding model and could in principle lead to the relative concentrations of the different chiralities in a given sample. However, in our case, the surface state of the NTs changes step after step, as evidenced by TEM, EELS and XRD. Thus an absolute determination of the relative distribution of a purified sample compared to another purified sample resulting from a different purification step is precluded. We therefore restricted ourselves to the following qualitative conclusion. When comparing the chirality distribution of the RBM intensities in the pristine nanotubes and sample **11**, it appears that almost all the modes that have decreased or increased upon purification represent semi-metallic nanotubes, whatever their diameter or chiral angle. The change in their intensity is most probably due to a change in their scattering cross section rather than to a selective combustion process. It further confirms that during the purification process, the surface of the nanotubes is chemically modified, consistently with the increased organization of the bundles observed by HAADF-STEM and XRD. This chemical change is mainly affecting the electronic structure of the semi-metallic nanotubes.

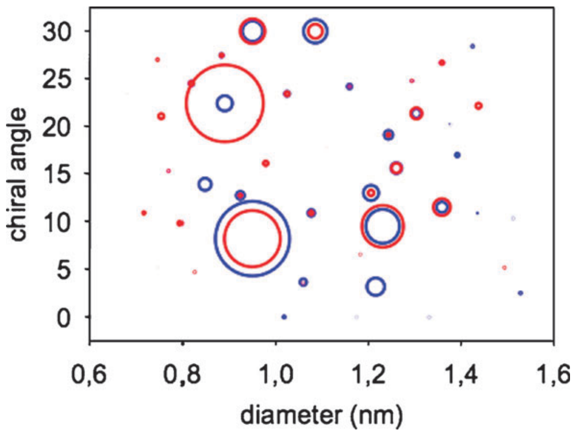

Fig. 23 Chirality distribution of the pristine (red circles) and **11** (blue circles) nanotubes.

Conclusions

Suggested general mechanism and possible improvements of the procedure

Catalytic impurities. Electronic microscopy experiments, EELS and magnetization measurements have shown that two populations of catalyst nanoparticles initially coexist in pristine nanotubes. One of them consists of isolated particles decorating the sidewalls of nanotubes bundles, with diameters of 3–6 and 10–20 nm, encapsulated in graphitic shells of various thicknesses. The other is composed of Fe_3C nanoparticles gathered into large bunches, with diameters ranging from 10 to 20 nm, that are encapsulated in multiple graphitic layers of 2–3 nm average thickness. The isolated particles are quantitatively eliminated after step **10** (450 °C) while the bunches of particles start to be damaged upon heating at 500 °C, with a noticeable subsequent carbon combustion. EELS and TEM analysis of the pristine nanotubes and of samples **3**, **8** and **15** have provided mechanistic evidences about the purification process. First, toroidal (hollow) particles consisting of an iron oxide internal layer and a graphitic external capsule are found until step **3**. Contradictory with what have been assumed previously, their presence shows that the metal-rich core is oxidized prior to the combustion of the carbon shell.[16] Second, until step **8**, isolated particles are found in oxidized or non-oxidized states, whatever their relative sizes. After step **10**, the remaining isolated particles belong to the 10–20 nm type. The heavily encapsulated particles belonging to bunches remain unoxidized the longest and are the last to be eliminated. These observations show that their is a distribution of reactivity towards oxidation within the particles, which can be understood in terms of the carbon shell thickness and curvature. The particles presenting low curvature and thick shells are more difficult to oxidize. Starting from these experimental observations, a new mechanism for the purification can be drawn. This involves the diffusion of the oxygen in the metal-rich core of the particle as the limiting step. The diffusion of a gas across a porous material is controlled by the ratio between the free rotation radius of the gas molecule and the size of the pores.[69] Assuming similar reactivities between graphitic shells and fullerenes, one can suggest three pathways for the diffusion of the oxygen towards the particles cores: (i) diffusion through slits between mismatching graphitic sheets of a non-continuous capsule; (ii) diffusion through large pores generated by vacancies in graphitic shells;[70] (iii) partial oxidation of graphitic shells, leading to the creation of ether oxide and carbonyl functions and diffusion of the oxygen through the subsequent larger pores.[71] Once a pathway is open for the oxygen to diffuse towards the core, the second step of the proposed mechanism involves the complete oxidation of the carbide phase. Eventually, the graphitic capsule is oxidized under iron oxide catalysis.

According to this mechanism, the thicker and the more regular the graphitic capsule, the more difficult the diffusion of the oxygen towards the core is. In addition, it has been demonstrated by calorimetric measurements that large fullerenes are partially oxidized at higher temperature than found for smaller ones.[72] Thus, the larger the particle, the higher the temperature needs to be raised to create an oxygen diffusion pathway. Consequently, the bunches of large particles encapsulated in thick multiple graphitic layers can be eliminated only at high temperatures. Unfortunately, such high temperatures lead to the fast combustion of the nanotubes decreasing dramatically the yield of the last purification steps. Thus, after steps **8** and **9** where most of the iron has been removed (Fig. 1 and Table 1), it would be wiser to use a complementary method to get rid of the large particles. As these large particles belong to bunches of around 100 nm in size and are well localized in the purified samples, we suggest to further purify the nanotubes using a magnetic segregation method.[73–75]

Carbon and silicon impurities. HAADF-STEM and XRD experiments have demonstrated an increase of the organization within the bundles of nanotubes along the purification process, that has been attributed to a removal of some carbonaceous impurity from the sidewalls of the nanotubes. A partial removal of carbonaceous impurities has been further evidenced by analysis of the Raman D-mode. Eventually, EELS measurements have shown that after the overall purification procedure, a thin layer of amorphous carbon remains on the sidewall of the nanotubes, associated with a silicon pollution. These surface coverings of the nanotubes may affect their dispersability, electronic properties and cytotoxicity. To access the true properties and reactivity of the nanotubes in further design of SWNTs composites, carbon and silicon impurities should be removed by complementary procedures. We observed (Fig. S13, ESI†) that this can be successfully achieved by combining an annealing under argon and a reflux in concentrated sodium hydroxide aqueous solution, using previously reported procedures.[44,76]

References

1 R. H. Baughman, A. A. Zakhidov and W. A. de Heer, *Science*, 2002, **297**, 787–792.
2 R. J. Chen, S. Bangsaruntip, K. A. Drouvalakis, N. W. S. Kam, M. Shim, Y. M. Li, W. Kim, P. J. Utz and H. J. Dai, *Proc. Natl. Acad. Sci. U. S. A.*, 2003, **100**, 4984–4989.
3 J. Kong, N. R. Franklin, C. W. Zhou, M. G. Chapline, S. Peng, K. J. Cho and H. J. Dai, *Science*, 2000, **287**, 622–625.
4 C. Staii and A. T. Johnson, *Nano Lett.*, 2005, **5**, 1774–1778.
5 L. D. Zhu, J. L. Zhai, Y. N. Guo, C. Y. Tian and R. L. Yang, *Electroanalysis*, 2006, **18**, 1842–1846.
6 Y. Guo, D. L. Shi, H. S. Cho, Z. Y. Dong, A. Kulkarni, G. M. Pauletti, W. Wang, J. Lian, W. Liu, L. Ren, Q. Q. Zhang, G. K. Liu, C. Huth, L. M. Wang and R. C. Ewing, *Adv. Funct. Mater.*, 2008, **18**, 2489–2497.
7 Z. Liu, M. Winters, M. Holodniy and H. J. Dai, *Angew. Chem., Int. Ed.*, 2007, **46**, 2023–2027.
8 S. Polizu, O. Savadogo, P. Poulin and L. Yahia, *J. Nanosci. Nanotechnol.*, 2006, **6**, 1883–1904.
9 J. Appenzeller, J. Knoch, V. Derycke, R. Martel, S. Wind and P. Avouris, *Phys. Rev. Lett.*, 2002, 126801.
10 D. S. Hecht, R. J. A. Ramirez, M. Briman, E. Artukovic, K. S. Chichak, J. F. Stoddart and G. Gruner, *Nano Lett.*, 2006, **6**, 2031–2036.
11 D. E. Johnston, M. F. Islam, A. G. Yodh and A. T. Johnson, *Nat. Mater.*, 2005, **4**, 589–592.
12 G. Robert, V. Derycke, M. F. Goffman, S. Lenfant, D. Vuillaume and J. P. Bourgoin, *Appl. Phys. Lett.*, 2008, **93**, 3.
13 V. Pichot, S. Badaire, P. A. Albouy, C. Zakri, P. Poulin and P. Launois, *Phys. Rev. B: Condens. Matter Mater. Phys.*, 2006, 245416.
14 M. M. J. Treacy, T. W. Ebbesen and J. M. Gibson, *Nature*, 1996, **381**, 678–680.
15 B. Vigolo, A. Penicaud, C. Coulon, C. Sauder, R. Pailler, C. Journet, P. Bernier and P. Poulin, *Science*, 2000, **290**, 1331–1334.
16 I. W. Chiang, B. E. Brinson, A. Y. Huang, P. A. Willis, M. J. Bronikowski, J. L. Margrave, R. E. Smalley and R. H. Hauge, *J. Phys. Chem. B*, 2001, **105**, 8297–8301.
17 I. W. Chiang, B. E. Brinson, R. E. Smalley, J. L. Margrave and R. H. Hauge, *J. Phys. Chem. B*, 2001, **105**, 1157–1161.
18 A. C. Dillon, T. Gennett, K. M. Jones, J. L. Alleman, P. A. Parilla and M. J. Heben, *Adv. Mater.*, 1999, **11**, 1354–1358.
19 Y. C. Feng, G. M. Zhou, G. P. Wang, M. Z. Qu and Z. L. Yu, *Chem. Phys. Lett.*, 2003, **375**, 645–648.
20 A. R. Harutyunyan, B. K. Pradhan, J. P. Chang, G. G. Chen and P. C. Eklund, *J. Phys. Chem. B*, 2002, **106**, 8671–8675.
21 H. Hu, B. Zhao, M. E. Itkis and R. C. Haddon, *J. Phys. Chem. B*, 2003, **107**, 13838–13842.
22 M. N. Tchoul, W. T. Ford, G. Lolli, D. E. Resasco and S. Arepalli, *Chem. Mater.*, 2007, **19**, 5765–5772.
23 E. Vazquez, V. Georgakilas and M. Prato, *Chem. Commun.*, 2002, 2308–2309.
24 Y. H. Wang, H. W. Shan, R. H. Hauge, M. Pasquali and R. E. Smalley, *J. Phys. Chem. B*, 2007, **111**, 1249–1252.
25 J. G. Wiltshire, A. N. Khlobystov, L. J. Li, S. G. Lyapin, G. A. D. Briggs and R. J. Nicholas, *Chem. Phys. Lett.*, 2004, **386**, 239–243.
26 Y. Q. Xu, H. Q. Peng, R. H. Hauge and R. E. Smalley, *Nano Lett.*, 2005, **5**, 163–168.
27 M. Zhang, M. Yudasaka and S. Iijima, *J. Phys. Chem. B*, 2004, **108**, 149–153.
28 C. E. Banks, A. Crossley, C. Salter, S. J. Wilkins and R. G. Compton, *Angew. Chem., Int. Ed.*, 2006, **45**, 2533–2537.
29 X. Dai, G. G. Wildgoose and R. G. Compton, *Analyst*, 2006, **131**, 901–906.
30 T. Kolodiazhnyi and M. Pumera, *Small*, 2008, **4**, 1476–1484.
31 B. Sljukic, C. E. Banks and R. G. Compton, *Nano Lett.*, 2006, **6**, 1556–1558.
32 J. H. Choi, F. T. Nguyen, P. W. Barone, D. A. Heller, A. E. Moll, D. Patel, S. A. Boppart and M. S. Strano, *Nano Lett.*, 2007, **7**, 861–867.
33 M. A. Correa-Duarte, M. Grzelczak, V. Salgueirino-Maceira, M. Giersig, L. M. Liz-Marzan, M. Farle, K. Sierazdki and R. Diaz, *J. Phys. Chem. B*, 2005, **109**, 19060–19063.
34 C. Bussy, J. Cambedouzou, S. Lanone, E. Leccia, V. Heresanu, M. Pinault, M. Mayne-l'Hermite, N. Brun, C. Mory, M. Cotte, J. Doucet, J. Boczkowski and P. Launoist, *Nano Lett.*, 2008, **8**, 2659–2663.
35 K. Donaldson, *Toxicol. Sci.*, 2006, **92**, 5–22.
36 N. Lewinski, V. Colvin and R. Drezek, *Small*, 2008, **4**, 26–49.
37 M. E. Itkis, D. E. Perea, R. Jung, S. Niyogi and R. C. Haddon, *J. Am. Chem. Soc.*, 2005, **127**, 3439–3448.

38 After each step until step **11**, the amount of extracted iron was determined by visible spectroscopy titration from the 365 nm band of the $[FeCl_4]^-$ species present in the washing filtrate. For the subsequent steps, this titration could not been performed because the concentration of iron was too low.
39 M. Pumera, *Langmuir*, 2007, **11**, 6453–6458.
40 L. A. J. Garvie and P. R. Buseck, *Nature*, 1998, **396**, 667–670.
41 J. Gavillet, A. Loiseau, F. Ducastelle, S. Thair, P. Bernier, O. Stephan, J. Thibault and J. C. Charlier, *Carbon*, 2002, **40**, 1649–1663.
42 F. M. F. de Groot, M. Grioni, J. C. Fuggle, J. Ghijsen, G. A. Sawatzky and H. Petersen, *Phys. Rev. B: Condens. Matter Mater. Phys.*, 1989, **40**, 5715.
43 O. Stephan, M. Kociak, L. Henrard, K. Suenaga, A. Gloter, M. Tence, E. Sandre and C. Colliex, *J. Electron Spectrosc. Relat. Phenom.*, 2001, **114**, 209–217.
44 C. G. Salzmann, S. A. Llewellyn, G. Tobias, M. A. H. Ward, Y. Huh and M. L. H. Green, *Adv. Mater.*, 2007, **19**, 883–887.
45 J. Chatterjee, Y. Haik and C. J. Chen, *J. Magn. Magn. Mater.*, 2003, **257**, 113–118.
46 J. Murbe, A. Rechtenbach and J. Topfer, *Mater. Chem. Phys.*, 2008, **110**, 426–433.
47 B. David, N. Pizurova, O. Schneeweiss, P. Bezdicka, I. Morjan and R. Alexandrescu, *J. Alloys Compd.*, 2004, **378**, 112–116.
48 A. Kouprine, F. Gitzhofer, M. Boulos and T. Veres, *Carbon*, 2006, **44**, 2593–2601.
49 R. Sergiienko, E. Shibata, Z. Akase, H. Suwa, T. Nakamura and D. Shindo, *Mater. Chem. Phys.*, 2006, **98**, 34–38.
50 J. N. Wang, L. Zhang, F. Yu and Z. M. Sheng, *J. Phys. Chem. B*, 2007, **111**, 2119–2124.
51 D. W. Lee, J. H. Yu, B. K. Kim and T. S. Jang, *J. Alloys Compd.*, 2008, **449**, 60–64.
52 A. Shavel, B. Rodriguez-Gonzalez, M. Spasova, M. Farle and L. M. Liz-Marzan, *Adv. Funct. Mater.*, 2007, **17**, 3870–3876.
53 V. Heresanu, C. Castro, J. Cambedouzou, M. Pinault, O. Stephan, C. Reynaud, M. Mayne-L'Hermite and P. Launois, *J. Phys. Chem. C*, 2008, **112**, 7371–7378.
54 S. Rols, R. Almairac, L. Henrard, E. Anglaret and J. L. Sauvajol, *Eur. Phys. J. B*, 1999, **10**, 263–270.
55 A. C. Ferrari and J. Robertson, *Phys. Rev. B: Condens. Matter Mater. Phys.*, 2001, 075414.
56 C. Thomsen and S. Reich, *Phys. Rev. Lett.*, 2000, **85**, 5214–5217.
57 M. A. Pimenta, A. Jorio, S. D. M. Brown, A. G. Souza, G. Dresselhaus, J. H. Hafner, C. M. Lieber, R. Saito and M. S. Dresselhaus, *Phys. Rev. B: Condens. Matter Mater. Phys.*, 2001, 041401.
58 A. C. Dillon, P. A. Parilla, J. L. Alleman, T. Gennett, K. M. Jones and M. J. Heben, *Chem. Phys. Lett.*, 2005, **401**, 522–528.
59 K. E. Hurst, A. C. Dillon, D. A. Keenan and J. H. Lehman, *Chem. Phys. Lett.*, 2007, **433**, 301–304.
60 M. S. Dresselhaus, G. Dresselhaus and M. Hofmann, *Vib. Spectrosc.*, 2007, **45**, 71–81.
61 M. S. Dresselhaus, G. Dresselhaus, A. Jorio, A. G. Souza and R. Saito, *Carbon*, 2002, **40**, 2043–2061.
62 H. Son, A. Reina, G. G. Samsonidze, R. Saito, A. Jorio, M. S. Dresselhaus and J. Kong, *Phys. Rev. B: Condens. Matter Mater. Phys.*, 2006, 073406.
63 H. B. Son, A. Reina, M. S. Dresselhaus and J. Kong, *Phys. Status Solidi B*, 2006, **243**, 3161–3165.
64 R. Bhowmick, B. M. Clemens and B. A. Cruden, *Carbon*, 2008, **46**, 907–922.
65 Y. Miyata, T. Kawai, Y. Miyamoto, K. Yanagi, Y. Maniwa and H. Kataura, *J. Phys. Chem. C*, 2007, **111**, 9671–9677.
66 M. Machon, S. Reich, H. Telg, J. Maultzsch, P. Ordejon and C. Thomsen, *Phys. Rev. B: Condens. Matter Mater. Phys.*, 2005, 035416.
67 V. N. Popov, L. Henrard and P. Lambin, *Nano Lett.*, 2004, **4**, 1795–1799.
68 Y. Yin, A. N. Vamivakas, A. G. Walsh, S. B. Cronin, M. S. Unlu, B. B. Goldberg and A. K. Swan, *Phys. Rev. Lett.*, 2007, 037404.
69 K. P. Travis, *Mol. Phys.*, 2002, **100**, 2317–2329.
70 Y. H. Hu and E. Ruckenstein, *J. Chem. Phys.*, 2003, **119**, 10073–10080.
71 M. Wohlers, H. Werner, D. Herein, T. SchedelNiedrig and A. Bauer, *Synth. Met.*, 1996, **77**, 299–302.
72 A. Rojas, M. Martinez, P. Amador and L. A. Torres, *J. Phys. Chem. B*, 2007, **111**, 9031–9035.
73 J. H. Kang and J. K. Park, *Small*, 2007, **3**, 1784–1791.
74 Y. Kim and D. E. Luzzi, *J. Phys. Chem. B*, 2005, **109**, 16636–16643.
75 J. G. Wiltshire, L. J. Li, A. N. Khlobystov, C. J. Padbury, G. A. D. Briggs and R. J. Nicholas, *Carbon*, 2005, **43**, 1151–1155.
76 M. Monthioux, B. W. Smith, B. Burteaux, A. Claye, J. E. Fischer and D. E. Luzzi, *Carbon*, 2001, **39**, 1251–1272.